Materials Today Bio 31 (2025) 101547

Contents lists available at ScienceDirect

Materials Today Bio

journal homepage: www.journals.elsevier.com/materials-today-bio

Nanozyme based ultra-stretchable, low-hysteresis, and dual-mode antibacterial composite hydrogels for wound healing

Yanyan Li[a,1], Weiqi Kang[b,1], Jian Zhang[a], Ping Shi[b,**], Jianshu Li[c,d,***], Yongping Lu[b,*]

[a] College of Chemistry and Chemical Engineering, Shanxi University, Taiyuan, 030006, PR China
[b] Scientific and Technological Innovation Center for Biomedical Materials and Clinical Research, Guangyuan Key Laboratory of Multifunctional Medical Hydrogel, Guangyuan Central Hospital, Guangyuan, 628000, PR China
[c] College of Polymer Science and Engineering, State Key Laboratory of Polymer, Sichuan University, Chengdu, 610041, PR China
[d] State Key Laboratory of Oral Diseases, West China Hospital of Stomatology, Sichuan University, Chengdu, 610041, PR China

ARTICLE INFO

Keywords:
Dynamic micelle
Low-hysteresis
Peroxidase and oxidase mimics
Photothermal effect
Dual-mode antibacterial

ABSTRACT

Wound care always presents challenges as they are susceptible to bacterial infections and have mechanical compatibility issues with wound dressings, leading to a delayed recovery of the structure and functional integrity of skin tissue. Herein, an iron-based metal-organic framework loaded with gold (Fe-MIL-88NH_2-Au) nanozyme based composite hydrogel (HMAux) with excellent mechanical compatibility and dual-mode antibacterial properties was designed for wound care. To obtain HMAux, Fe-MIL-88NH_2-Au nanozyme with photothermal properties and peroxidase-like and oxidase-like activities was prepared. Then it was introduced into the hydrogel system with a sea-island structure which was prepared *via* the copolymerization of acrylamide and acryloyl Pluronic F127 (PF127-DA) in the aqueous solution. Using dynamic micelles as the energy dissipation mechanism, double bonds and intermolecular interactions as two crosslinking methods in HMAux make it possess good stretchability (3244 %–4524 %), toughness (593.8 kJ/m^3 to 421.5 kJ/m^3), and low hysteresis (0.13–0.15). Furthermore, the synergistic photothermal and chemodynamic effects provide good antibacterial performance under mild conditions, with killing rates of approximately 95.02 % and 97.28 % for *S. aureus* and *E. coli*, respectively. *In vivo* experiments have proved that HMAux can effectively adapt to the contour of the wound and treat wound infections.

1. Introduction

Wounds impose significant burdens on both patients and healthcare systems, making wound care a concerning and increasingly common issue on the global scale [1,2]. As is well known, wound healing is a complex and well-coordinated process, including inflammation, proliferation, and remodeling [3,4]. The use of wound dressings can significantly improve the repair process of wounds [5,6]. Therefore, developing effective wound dressings has enormous potential for preventing adverse consequences and accelerating tissue renewal and regeneration [7,8]. Global skin wound dressings will be a key component of the wound care industry, with a market size of $5.05 billion in 2024 [9,10]. Designing and developing advanced wound dressings have become one of the central focuses in the biomedical field [11]. Researchers are conducting extensive studies to develop dressings that can effectively treat wounds and promote healing in a short period of time to improve comfort of patients.

Among the variety of wound dressings, hydrogels have irreplaceable advantages in wound healing due to their high water content, substantial porosity, pliability, excellent biocompatibility, mechanical properties that can be adjusted, and easily functionalized, having received widespread attention [12–14]. In recent years, many researches have been devoted to the preparation of hydrogels with excellent mechanical properties to achieve the best mechanical compatibility between the

---

* Corresponding author.
** Corresponding author.
*** Corresponding author. College of Polymer Science and Engineering, State Key Laboratory of Polymer, Sichuan University, Chengdu, 610041, PR China
E-mail addresses: cgscshiping@163.com (P. Shi), jianshu_li@scu.edu.cn (J. Li), luyongping_lyp@163.com (Y. Lu).
[1] These authors contributed equally to this work.

https://doi.org/10.1016/j.mtbio.2025.101547
Received 10 December 2024; Received in revised form 22 January 2025; Accepted 2 February 2025
Available online 3 February 2025

dressing and the surrounding tissues of the wound and to meet the needs of daily wound care while ensuring comfort as far as possible [15,16]. It is not difficult to find that the design of material structure and energy dissipation mechanism by adjusting synthetic raw materials and cross-linking methods, such as introducing sacrificial bonds, fillers, or secondary networks, can effectively avoid the shortcomings of low strength and poor toughness of traditional hydrogels to obtain a hydrogel with good mechanical properties liking double network hydrogels, topological hydrogels, composite hydrogels, ion bonded hydrogels and hybrid hydrogels [17–20]. However, these strategies usually give rise to hydrogels with large hysteresis and fatigue damage [17], which is far from achieving the best mechanical match between the dressing and the tissue around the wound. This will cause the separation of the dressings and the wounds or wounds tightness, greatly affecting comfort.

In addition to considering the comfort of the surrounding wound tissue, the antibacterial performance of dressings should also be emphasized in wound care, as bacteria are almost ubiquitous and there is a high risk of infection in the wound [21]. Wound infection induced by pathogenic bacteria is the main cause of delayed healing and may lead to life-threatening complications, which has caused substantial economic losses and considerable threats to global health [22]. For most types of bacteria, high temperature and reactive oxygen species (ROS) can cause protein denaturation and structural damage, leading to death [23,24]. Photothermal therapy (PTT) based on nanomaterials generates a large amount of physical heat during near-infrared laser irradiation, which has attracted much attention for antibacterial applications. This strategy is easy to operate, not prone to drug resistance, and fewer side effects, having broad-spectrum antibacterial characteristics [4,25,26]. And chemodynamic therapy (CDT) generates ROS to kill bacteria, with advantages similar to those of PTT [27]. However, local high temperatures associated with PTT may damage surrounding wholesome cells and tissues when killing bacteria, and CDT may require higher concentrations of hydrogen peroxide and more stringent conditions [28,29]. The combination of PTT and CDT can exert a synergistic effect, killing bacteria at lower temperatures and the presence of low concentrations of hydrogen peroxide, which will effectively avoid the troubles that exist when treated separately by PTT or CDT.

Nanomaterials typically have multiple functions, such as antibacterial, antioxidant, and photothermal properties [30,31]. Nanozymes are nanomaterials with enzyme-like catalytic properties, thus using nanozymes as functional components is expected to achieve the integration of PTT and CDT [32]. Iron based metal-organic frameworks (MOFs) nanozymes are nanomaterials with a framework structure formed by iron ions and organic ligands, exhibiting excellent catalytic activity [33]. For example, our previous research has shown that Fe-MIL-88NH$_2$ can simulate both peroxidase and oxidase, producing hydroxyl radicals and superoxide anions during catalytic reactions [34]. Both types of ROS have strong oxidative damage effects on bacterial structures. We also discovered that Fe-MIL-88NH$_2$ nanozyme has good biocompatibility. The iron ions in Fe-MIL-88NH$_2$ nanozyme can be stored and processed by the human body. In addition, the framework structure of Fe-MIL-88NH$_2$ also allows to load other components to exert more functions. Integrating Fe-MIL-88NH$_2$ with photothermal materials is a very attractive strategy for a combination PTT and CDT to combat bacteria.

Herein, Fe-MIL-88NH$_2$ with octahedral morphology was synthesized using the solvothermal method, and gold nanoparticles (Au) grown were grown *in situ* on the surface of Fe-MIL-88NH$_2$ by reducing chloroauric acid with sodium borohydride to obtain the Fe-MIL-88NH$_2$-Au nanozyme with photothermal properties and peroxidase-like and oxidase-like activities (Fig. 1Aa). Then, double bond terminated PF127-DA was synthesized and used as a cross-linking agent (Fig. 1Ab) to polymerize with acrylamide in an aqueous solution to prepare the black hydrogel. The target hydrogel HMAux was obtained by introducing Fe-MIL-88NH$_2$-Au nanozyme in the preparation process of black hydrogel (Fig. 1Ac). The prepared HMAux presented good stretchability (3244 %–4524 %), toughness (593.8 kJ/m^3 to 421.5 kJ/m^3), and low hysteresis (13.46 %–14.75 %), which is due to the use of dynamic micelles as the energy dissipation mechanism, and double bonds and intermolecular interactions as two crosslinking methods. Furthermore, the synergistic effects of PTT and CDT in HMAux allowed them to exhibit good antibacterial performance under mild conditions (Fig. 1B). We demonstrated that HMAux had a killing rate of approximately 95.02 % against *S. aureus* and about 97.28 % against *E. coli*. Additionally, *in vivo* experiments had proved that HMAux had good biocompatibility and could effectively adapt to the contour of the wound, treat wound infections, reduce levels of inflammatory factors, and promote cell proliferation, indicating its potential as a wound dressing to promote wound healing. The material designed by us can balance mechanical compatibility issues between wound dressing and wound, bacterial infection, and inflammation during the wound healing process.

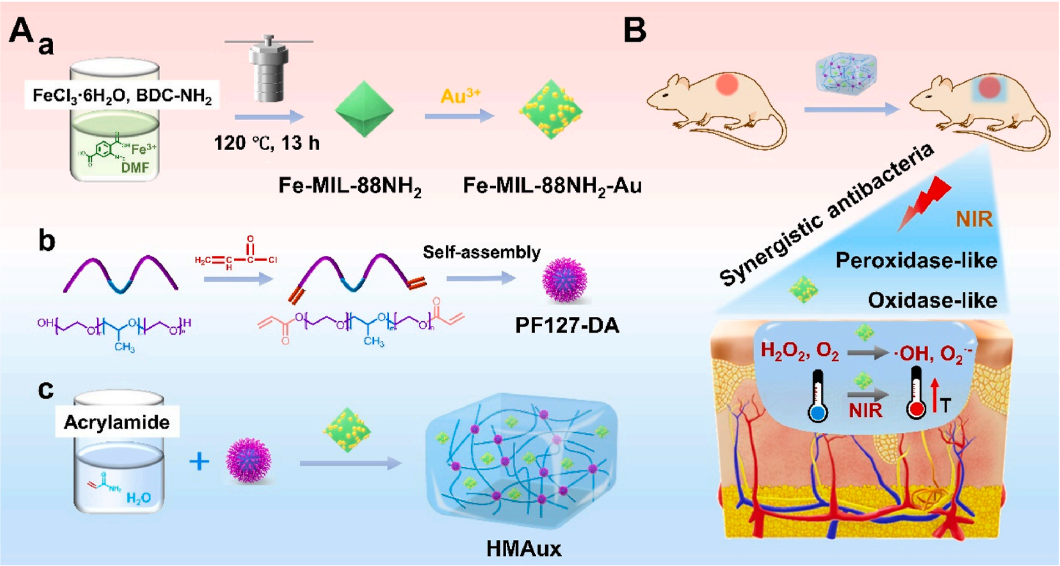

Fig. 1. (A) Schematic diagram of the fabrication process of HMAux. (B) The antibacterial mechanism of HMAux in an infected wound.

2. Experimental section

2.1. Synthesis of Fe-MIL-88NH$_2$-Au

Firstly, Fe-MIL-88NH$_2$ was prepared according to the reported method with slight modifications [35]. Briefly, 250.7 mg of 2-aminoterephthalic acid and 374.3 mg of ferric trichloride hexahydrate were dissolved in 30 mL dimethylformamide and sonicated for 30 min. The solution was transferred to a hydrothermal synthesis reactor and reacted at 120 °C for 13 h. Next, the pellets were collected by centrifugation at 8000 rpm after the reactor cooled to room temperature naturally. Then, the pellets were washed 3 times with dimethylformamide and ethanol respectively. Finally, the samples were dried in a vacuum oven at 40 °C to get the Fe-MIL-88NH$_2$.

100 mg of Fe-MIL-88NH$_2$ and 100 mL of deionized water were put into a beaker to obtain a 1 mg/mL mixture. The mixture was sonicated and dispersed, and then 4 mL of chloroauric acid at a concentration of 10 mM was added. After stirring for 3 min, 1 mL of sodium borohydride (100 mM) solution was added dropwise. The new pellets were collected by centrifugation at 8000 rpm after 30 min of reaction. Then, washed the pellets 3 times with ethanol. Finally, the Fe-MIL-88NH$_2$-Au nanozyme was dried in a vacuum oven at 40 °C for further characterization and application.

2.2. Synthesis of PF127-DA

PF127-DA was synthesized based on reference [36]. 2.54 g of PF127 was dissolved in 20 mL of dichloromethane in an ice bath, 85 μL of triethylamine was added, and nitrogen was ventilated for 20 min. Then, 50 μL of acryloyl chloride was added and the nitrogen was ventilated for 5 min continually. It reacted at room temperature for 24 h. The crude product was then obtained by removing the dichloromethane through rotary evaporation at 25 °C. The crude product was purified by dialysis for 3 days (MWCO 3500). Finally, the pure PF127-DA was obtained by lyophilization.

2.3. Synthesis of the HMAux

HMAux were prepared using APS/TEMED as the redox initiation system, PF127-DA as the crosslinker, and acrylamide as the monomer. Specifically, 105 mg PF127-DA, 300 mg of acrylamide, and a certain amount of deionized water were added to four tubes. Then the Fe-MIL-88NH$_2$-Au nanozyme was added to ensure that the content of acrylamide is 10 wt%, and the nanozyme is 0 mg/mL, 1 mg/mL, 1.5 mg/mL, or 2 mg/mL, respectively. Next, four tubes were sonicated until the reagents inside were completely dissolved and then pre-cooled in an ice bath. Then, 150 μL TEMED (100 μL/mL) and 150 μL APS (100 mg/mL) solutions were added sequentially under an ice bath. After that, the HMAux sample precursor was rapidly transferred to the mold and crosslinked at room temperature.

2.4. Characterizations

2.4.1. TEM

The structure of PF127-DA micelles was observed using a low-voltage TEM (HT7700, Hitachi Corp, Japan) with an accelerating voltage of 100 kV. TEM images and elemental analysis of Fe-MIL-88NH$_2$-Au nanozyme were recorded by FEI Talos F200x (Thermo Fisher Scientific, USA).

2.4.2. SEM

The microstructures and elemental analysis of HMAux were recorded by cryo-SEM (Apreo S HiVoc, Thermo Fisher Scientific, USA).

2.4.3. DLS

The particle sizes of Fe-MIL-88NH$_2$ nanozyme and Fe-MIL-88NH$_2$-Au nanozyme in deionized water were obtained by a protein particle size analyzer (Zetasizer μV, Malvern, Japan).

2.4.4. FTIR

The chemical structure of PF127-DA was confirmed by a Nicolet is50 FTIR (Thermo Fisher Corp, USA).

2.4.5. ^{1}H NMR

The chemical structure of PF127-DA was also confirmed by a Bruker AV III HD 400 MHz instrument with deuterated chloroform serving as the solvent and internal standards.

2.4.6. ESR

The generation of free radicals during the reaction process was confirmed using an ESR spectrometer (EMX Plus-6/1, Bruker Corp, Germany). The tests were conducted in sodium acetate buffer (0.1 M, pH 4). The concentrations of H_2O_2, DMPO, HMAu$_0$, and HMAu$_{1.5}$ are 100 μM, 50 mM, 50 mg/mL, and 50 mg/mL, respectively. After 30 min of reaction, the reaction solution was tested.

2.5. Mechanical performance tests

A tensile machine with a 10 N load cell (HZ-1004B, Dongguan Lixian Instrument Technology Co., Ltd.) was used to test the mechanical properties of HMAux samples. Experimental steps are described in details in the *Supporting Information*.

2.6. Enzyme mimetic activity

The peroxidase and oxidase mimic activities of Fe-MIL-88NH$_2$-Au nanozyme and HMAux samples were evaluated using a TMB chromogenic reaction according to reference [37]. To test the ability of HMAux samples to mimic peroxidase, the absorbance curves in the range of 360–750 nm after 30 min of reaction were monitored in spectral scanning mode. The concentrations of the HMAux sample, H_2O_2, and TMB were 50 mg/mL, 100 μM, and 1 mM. The ability of HMAux samples to simulate oxidase was also tested using the same method except for the absence of H_2O_2. Next, the optimal pH value was obtained by measuring the absorbance value of the Fe-MIL-88NH$_2$-Au nanozyme system at 652 nm after 15 min of reaction at different pH values using 0.1 M sodium acetate solution as a buffer system. And the optimal temperature was obtained by measuring the absorbance value of the Fe-MIL-88NH$_2$-Au nanozyme system at 652 nm after 15 min of reaction at different temperatures using 0.1 M sodium acetate solution as a buffer system. The absorbance value was measured by a UV spectrophotometer (Beijing Puxi General Instrument Co., Ltd., TU-1901, China). The concentrations of Fe-MIL-88NH$_2$-Au nanozyme, H_2O_2, and TMB were 50 g/mL, 100 μM, and 1 mM, respectively. When determining the optimal pH value and temperature of oxidase, H_2O_2 was not added, while the concentrations of other substances remained the same.

2.7. Photothermal performance

The photothermal properties of the HMAux samples were characterized by a near-infrared thermal imaging system (Testo, 885-2, Germany). Firstly, HMAux samples were purified in normal saline for 24 h. Then, 200 mg HMAux sample was placed in a tube and 300 μL of deionized water was added. The tube was irradiated with an 808 nm laser for 10 min and temperature values were recorded every 30 s. The temperature variation of the system at power densities of 1 W/cm^2, 1.5 W/cm^2, and 2.0 W/cm^2 was recorded. Finally, the photothermal cycling stability of the HMAu$_{1.5}$ sample at 1.5 W/cm^2 was investigated.

2.8. Antibacterial performance

Bacterial solutions of *S. aureus* and *E. coli* were diluted to 10^6 CFU/

mL with sodium acetate buffer (0.1 M, pH 4). Following that, 300 μL of diluted bacterial solution was co-incubated with 200 mg HMAux sample. The samples were divided into two major groups, totaling 24 analysis groups: *S. aureus* groups (without NIR: 1. PBS; 2. $HMAux_0$; 3. $HMAux_{1.5}$; 4. PBS + H_2O_2 (100 μM); 5. $HMAux_0$+H_2O_2 (100 μM); 6. $HMAux_{1.5}$+H_2O_2 (100 μM); with NIR: 7. PBS + NIR; 8. $HMAux_0$+NIR; 9. $HMAux_{1.5}$+NIR; 10. PBS + H_2O_2 (100 μM) + NIR; 11. $HMAux_0$+H_2O_2 (100 μM) + NIR; 12. $HMAux_{1.5}$+H_2O_2 (100 μM) + NIR) and *E. coli* groups (grouping consistent with *S. aureus*). For groups without NIR, HMAux samples were co-incubated with the bacterial solution for 180 min. For groups with NIR, HMAux samples were co-incubated with the bacterial solution for 170 min and then irradiated with the NIR laser (1.5 W/cm^2) for 10 min. Subsequently, the bacterial solution treated with the HMAux sample was diluted 10^4-fold and a 100 μL aliquot was placed on a solid medium for plate coating. The solid mediums were incubated at 37 °C for 9–12 h and then the number of colonies formed was recorded.

2.9. Cell compatibility tests

Mouse fibroblasts (L929) were cultured and passaged. Then L929 cells were seeded in 48-well plates at an initial density of 1.5×10^4 cells/well and cultured in the cell culture incubator for 24 h for subsequent experiments.

The HMAux samples with a diameter of 8 mm and a thickness of 2 mm were immersed in 75 % ethanol for 24 h for sterilization. Then the HMAux samples were soaked in saline and replaced with fresh saline every 1 h, repeating 5 times. After that, the sterilized HMAux samples were co-incubated with cells for 24 h, which was used for cellular vitality measurement, dead/live cell staining evaluation, and cell morphology assessment.

2.9.1. Cellular vitality

After the HMAux samples co-incubated with cells for 24 h, the cellular viability was quantitatively tested using the CCK-8 kit.

2.9.2. Dead/live cell staining evaluation

After the HMAux samples were co-incubated with cells for 24 h, the dead/live cell staining evaluation was performed using the live/dead staining kit. The stained cells were observed and recorded by a fluorescence microscope (green fluorescence: FDA for live cells, red fluorescence: PI for dead).

2.9.3. Cell morphology assessment

After the HMAux samples were co-incubated with cells for 24 h, the cell morphology was assessed. The cells were fixed with 4 % paraformaldehyde for 30 min, and then the fixed cells were treated with 0.2 % Triton X-100 for 5 min to change the permeability of the cell membrane. After that, the cells were stained with ghost pen cyclic peptide solution and 4′, 6-diamidino-2-phenylindole. The stained cells were observed and recorded by a fluorescence microscope.

2.10. Animal experiments

2.10.1. Animal modeling and treatment

Healthy male Kunming mice (25–30 g) were procured from the Chengdu DaShuo Experimental Animal Co., Ltd. The study received approval from the Animal Ethics Committee of Sichuan University (Animal Ethics No.: 2019067A). The mice were housed in polypropylene cages maintained at a standard temperature of 20 ± 4 °C. The mice were provided conventional feed and had unrestricted access to drinking water. A circular full-thickness skin wound, approximately 8 mm in diameter, was created on the neck of the mice to investigate the impact of the HMAux sample on wound repair at the wound site. Before the experiment, mice were acclimated to the laboratory environment for three days. The neck area was shaved and anesthesia was induced using 1 % pentobarbital sodium. The wound skin was sterilized with an iodophor solution and 4 % chlorhexidine gluconate before making the skin wound. A 10 μL solution of *S. aureus* (concentration: 10^8 CFU/mL) was applied to the wound to induce infection. The mice were divided into 8 groups (3 mice per group) for various treatments: 1. PBS; 2. $HMAux_0$; 3. $HMAux_{1.5}$; 4. $HMAux_{1.5}$+H_2O_2 (100 μM); 5. PBS + NIR; 6. $HMAux_0$+NIR; 7. $HMAux_{1.5}$+NIR; 8. $HMAux_{1.5}$+H_2O_2 (100 μM) + NIR. The progression of wound healing was documented through measurements and photographs on days 0, 2, 5, 8, and 11. The hydrogel samples were replaced during photography to capture the progress of the wound.

2.10.2. Histological analysis

All mice were euthanized on the 11th day, and relevant wound tissues and major organs (heart, liver, spleen, lungs, kidneys) were collected, fixed with 4 % formaldehyde, and embedded in paraffin. The samples were sliced and fixed on a glass slide to perform H&E staining for histological analysis.

2.10.3. Immunofluorometric assay

Immunofluorometric assays were conducted as described previously [38]. The primary antibody was IL-6 (1:100), and the fluorescently labeled secondary antibody was FITC-labeled goat anti-rabbit IgG (1:100).

2.11. Statistical analysis

Data in this manuscript from three individual experiments are described as mean ± standard deviation (mean ± SD). The statistical trends from different groups were analyzed by one-way ANOVA with post-test using Dunnett's test (GraphPad Prism 9.5.0). Data were considered as statistically significant difference if P-values were below 0.05 *versus* the indicated group ($^*P < 0.05$, $^{**}P < 0.01$ and $^{***}P < 0.001$).

3. Results and discussion

3.1. Synthesis and characterization of Fe-MIL-88NH_2-Au and HMAux

The Fe-MIL-88NH_2 nanozyme was first synthesized using the solvothermal method, and then chloroauric acid was reduced in the Fe-MIL-88NH_2 nanozyme mixture solution by sodium borohydride to prepare Fe-MIL-88NH_2-Au nanozyme. The morphology and structure of Fe-MIL-88NH_2-Au nanozyme were characterized using TEM and SEM, as shown in Fig. 2A and S1. The results of TEM, elemental analysis, and SEM showed that Fe-MIL-88NH_2 nanozyme successfully loaded Au nanoparticles, while the distribution of Au nanoparticles was not uniform, which had influenced the octahedra structure of Fe-MIL-88NH_2 nanozyme to some extent. The particle sizes of Fe-MIL-88NH_2 nanozyme and Fe-MIL-88NH_2-Au nanozyme in deionized water were also tested by DLS and the results revealed that the particle size of Fe-MIL-88NH_2-Au nanozyme is larger than that of the Fe-MIL-88NH_2 (Figure S2), which is consistent with the expected results.

Next, the enzyme-like activities of Fe-MIL-88NH_2-Au nanozyme were studied. As shown in Figure S3, Fe-MIL-88NH_2 nanozyme and Fe-MIL-88NH_2-Au nanozyme can oxidize TMB to ox-TMB in the presence of 100 μM H_2O_2, and an enhanced peak signal at 652 nm appears of Fe-MIL-88NH_2-Au nanozyme, demonstrating the peroxidase-like activity of Fe-MIL-88NH_2 nanozyme and Fe-MIL-88NH_2-Au nanozyme. Additionally, two types of nanozymes can also oxidize TMB to ox-TMB in the absence of H_2O_2, and an enhanced peak signal at 652 nm appears of Fe-MIL-88NH_2 nanozyme, indicating the oxidase-like activity of Fe-MIL-88NH_2 nanozyme and Fe-MIL-88NH_2-Au nanozyme. The above results also illustrate that the peroxidase-like activity of Fe-MIL-88NH_2-Au nanozyme is slightly stronger than that of Fe-MIL-88NH_2 nanozyme, while the oxidase-like activity shows the opposite trend.

Considering the effect of pH on the antimicrobial properties of

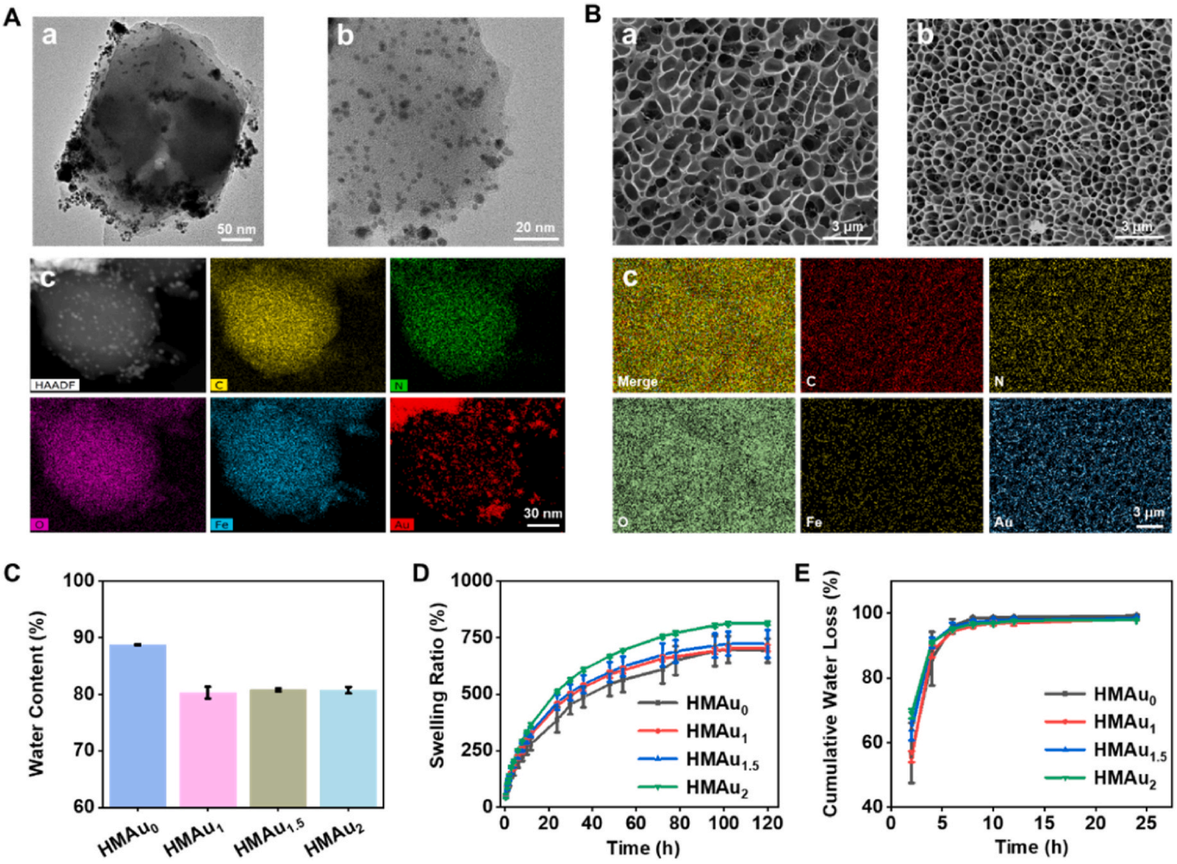

Fig. 2. Characterizations of Fe-MIL-88NH$_2$-Au and HMAux. (A) The images of TEM and elemental analysis of Fe-MIL-88NH$_2$-Au nanozyme: (a) and (b) TEM images, and (c) elemental mapping. (B) The images of SEM and elemental analysis of HMAux: (a) SEM image of HMAu$_0$, (b) SEM image of HMAu$_{1.5}$, and (c) elemental mapping of HMAu$_{1.5}$. (C) Water content, (D) swelling behaviors, and (E) cumulative water loss behaviors of different HMAux samples.

nanozyme-based antimicrobial materials, the dependence of the enzymatic activity of the developed nanozyme on pH was studied. Figure S4A shows the dependence of the peroxidase-like activity of Fe-MIL-88NH$_2$ and Fe-MIL-88NH$_2$-Au nanozymes on the pH of the system. The optimal pH for peroxidase-like activity of the two different nanozymes is 4 and the activity of Fe-MIL-MIL-88NH$_2$-Au nanozyme is higher, except at pH 3. Figure S4B illustrates the relationship between the oxidase-like activity of Fe-MIL-88NH$_2$ and Fe-MIL-88NH$_2$-Au nanozymes with the pH of the system, showing that the optimal pH for the latter is 3 and the activity is low. Overall, the pH dependence of the enzymatic activities of the two nanozymes differed. However, the enzymatic activity of Fe-MIL-88NH$_2$ nanozyme was not significantly affected by the loading of Au nanoparticles. The temperature dependence of the enzymatic activity of Fe-MIL-88NH$_2$-Au nanozyme was also studied. As shown in Figure S5, the optimal temperature of the peroxidase-like and oxidase-like activities of Fe-MIL-MIL-88NH$_2$-Au nanozyme is about 35 °C, which is beneficial for *in vivo* applications.

After preparing the Fe-MIL-88NH$_2$-Au nanozyme, we synthesized PF127 with double bond capping (PF127-DA) as a crosslinking agent for preparing HMAux. PF127 is a typical amphiphilic triblock copolymer (polyoxyethylene-polyoxypropylene-polyoxyethylene: PEO$_{99}$-PPO$_{65}$-PEO$_{99}$) that easily forms micelles in water through self-assemble, which is particularly advantageous for energy dissipation [39]. The chemical structure of PF127-DA was confirmed by fourier-transform infrared (FTIR) and proton nuclear magnetic resonance (^{1}H NMR). As shown in Figure S6, the new absorption peak appeared at 1722 cm^{-1}, which belongs to the stretching vibration of C=O, proving the successful synthesis of PF127-DA. The spectrogram of ^{1}H NMR presented characteristic chemical shifts at 6.4 and 5.9 ppm (Figure S7), which is attributed to the hydrogen on the double bond of acrylic ester, confirming the synthesis of PF127-DA once again [36]. Furthermore, the formation of PF127-DA micelles in water was confirmed by TEM (Figure S8).

Subsequently, we prepared HMAux samples using acrylamide as the monomer, PF127-DA as the crosslinking agent, and the Fe-MIL-88NH$_2$-Au nanozyme as a functional additive, where x presents the concentration of the added nanozyme. The microscopic topographies of HMAu$_0$ and HMAu$_{1.5}$ were characterized. As shown in SEM images in Fig. 2Ba and b, the microscopic topographies of HMAu$_0$ and HMAu$_{1.5}$ are both uniform three-dimensional porous. We counted the pore size of HMAu$_0$ and HMAu$_{1.5}$. The results are shown in Figure S9. The average pore size of HMAu$_0$ is about 0.88 μm, while the average pore size of HMAu$_{1.5}$ is about 0.50 μm, which is smaller than that of the HMAu$_0$. We also characterized the location of Fe-MIL-88NH$_2$-Au nanozyme within HMAu$_{1.5}$ by the elemental mapping. The result was shown in Fig. 2Bc, concluding that Fe-MIL-88NH$_2$-Au nanozyme was evenly distributed in HMAu$_{1.5}$. To analyze the reason for the average pore size in HMAu$_0$ larger than HMAu$_{1.5}$, we tested the water content of different HMAux samples and found that HMAu$_0$ had a higher water content than other samples (Fig. 2C). It is precisely due to the high water content that the pore structure of HMAu$_0$ is relatively large. Next, the swelling behavior of the HMAux samples in water or simulated wound fluid was evaluated. The experimental results are shown in Fig. 2D and S10, where the swelling equilibrium of HMAu$_0$, HMAu$_1$, HMAu$_{1.5}$, and HMAu$_2$ in water reaches after 120 h, with the swelling rates of 692.3 %, 703.2 %, 722.3 %, and 814.3 %, respectively. Therefore, the swelling degree of HMAux increases with increasing content of Fe-MIL-88NH$_2$-Au nanozyme in the hydrogel, which may be related to the hydrophilic groups, such as amino and carboxyl groups on the surface of Fe-MIL-88NH$_2$-Au nanozyme [40]. However, the maximum swelling value of HMAux in simulated wound fluid is reached after 10 h and the maximum swelling ratio of $HMAu_0$, $HMAu_1$, $HMAu_{1.5}$, and $HMAu_2$ is about 317.8 %, 340.4 %, 314.4 % and 326.5 % respectively, fully demonstrate that they could absorb wound exudates. After 10 h, HMAux gradually loosened until their completely disappeared in the simulated wound fluid. This phenomenon is caused by the adsorbing of protein and salts by HMAux in the simulated wound fluid. We also measured the cumulative water loss behaviors of different HMAux samples. As presented in Fig. 2E, the cumulative water loss rates of the HMAux samples exceed 80 % after 5 h in an oven at 37 °C, indicating poor water retention performance of HMAux samples.

3.2. Mechanical behavior of HMAux

After successfully preparing HMAux, their mechanical behavior was characterized. We presented the mechanical properties of HMAux, selecting $HMAu_{1.5}$ as a representative sample. As shown in Fig. 3A, the $HMAu_{1.5}$ has good tensile and compressive properties, which can pull even several times its own size or be compressed to a very small volume without breaking, indicating excellent elasticity and toughness. Subsequently, the mechanical properties of HMAux were quantitatively measured. Fig. 3B shows the tensile stress-strain curves of HMAux, with the fracture strain decreasing from ~4524 % to ~3244 % and tensile strength increasing from ~449 kPa to 627 kPa and then decreasing to 493 kPa as the nanozyme content increases from 1.0 mg/mL to 2.0 mg/mL (Fig. 3C). While under the same strain, the stress of the sample increases as the increases of nanozyme content. This is because nanozyme as fillers can enhance materials, but also increase internal defects leading to a decrease in strain. When HMAux is subjected to an external force, the PF127-DA dynamic cross-linking structure can dissipate a lot of energy during deformation, thus presenting the excellent tensile properties of the samples. Fig. 3D shows Young's modulus of HMAux, which increases from ~0.53 kPa to ~4.38 kPa with increasing nanozyme content from 1.0 to 2.0 mg/mL. The results of high stretchability and low modulus indicate its good elasticity. Fig. 3E presents the toughness of HMAux, observed that the toughness decreases from 593.8 kJ/m^3 to 421.5 kJ/m^3 when the nanozyme content increases from 1.0 mg/mL to 2.0 mg/mL. Such high toughness is mainly due to the flexibility of the polyether chain and the unwrapping or slippage of the hydrophobic segments, which gives PF127-DA micelles good energy dissipation capacity [41]. However, the decrease in toughness with the increase of nanozyme content within HMAux is also due to the increase in internal defects caused by the nanozyme.

Tensile loading-unloading cycle tests were performed to investigate the fatigue damage of HMAux. As shown in Fig. 3E and S11, the HMAux exhibits a slight hysteresis and a negligible stress drop over 10 consecutive cycles under different strains, without exhibiting the fatigue damage characteristics of ordinary hydrogels. From the first loading-unloading curve of the tensile cycle test, the hysteresis of $HMAu_{1.5}$ is calculated to be 14.75 %, 14.27 %, and 13.46 % at a strain of 300 %, 500 %, and 700 %, respectively. The apparent hysteresis caused by sacrificial bonds can be avoided by introducing dynamic micelles [16]. Such a low

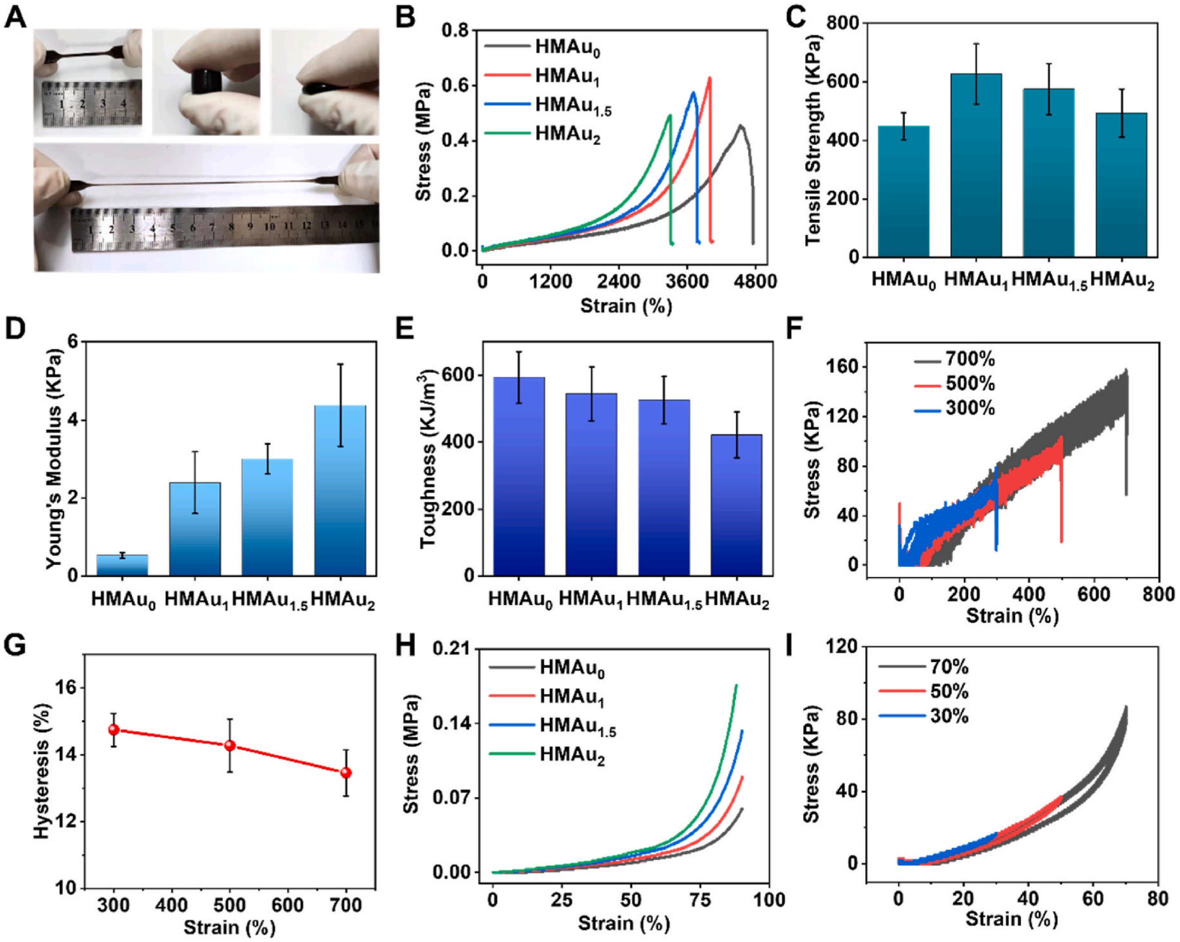

Fig. 3. Mechanical behavior of HMAux. (A) Displaying stretching and compressing images of $HMAu_{1.5}$. (B) Tensile stress-strain curves, (C) tensile strengths, (D) Young's modulus, and (E) toughnesses of different HMAux samples. (F) Cyclic tensile stress-strain cycle curves of $HMAu_{1.5}$ up to different maximum strains and (G) the corresponding hysteresis. (H) Compressive stress-strain curves of HMAux samples. (I) Cyclic compressive stress-strain curves of $HMAu_{1.5}$ up to different maximum strains.

hysteresis fully proves the elasticity of HMAux. As shown in Figure S12, HMAux exhibits both high toughness and low hysteresis, which breaks the traditional positive correlation between toughness and hysteresis [42–47]. In addition, when the strain in the compression test reaches 90 %, all HMAux samples could withstand extreme deformation without being damaged and returned to about 97 % of their initial height when the external force was removed (Fig. 3H), showing excellent elasticity. Furthermore, successive cyclic compression tests on $HMAu_{1.5}$ showed only slight hysteresis and negligible stress drops during 10 consecutive load-unload cycles under different strains (Fig. 3I and S13), which also demonstrated the elastomeric properties of HMAux. The PF127-DA micelle dynamic macromolecular crosslinker as stress absorbers subjected to large mechanical deformations, their deformation and internal rearrangement are undoubtedly an excellent energy dissipation mechanism, endowing HMAux with significant fatigue resistance and good elasticity [48–50]. Through this strategy, the traditional toughness-hysteresis correlation can overcome, simultaneously achieving high toughness and low hysteresis.

3.3. *Photothermal performance and enzyme mimicking properties of HMAux*

The photothermal properties of HMAux samples enable the conversion of light energy into thermal energy. As shown in Fig. 4A, using an 808 nm laser to irradiate a tube containing the HMAux sample and bacterial solution increases the temperature inside the tube, which can destroy bacteria and achieve disinfection. To evaluate the photothermal performance of HMAux samples, tubes containing HMAux samples and deionized water were irradiated with 808 nm lasers, and the temperature of the tubes was recorded every 30 s for a total of 10 min by the thermal imaging camera. Thermal images at the initial and terminal states of tubes containing $HMAu_0$ and $HMAu_{1.5}$ are shown in Fig. 4B. After 10 min of irradiation with 808 nm laser (1.5 W/cm^2), the temperature of the tube containing $HMAu_0$ increases from 23.5 °C to 24.0 °C, while the temperature of the tube containing $HMAu_{1.5}$ increases from 23.6 °C to 49.3 °C, fully demonstrating the excellent photothermal performance of $HMAu_{1.5}$. Subsequently, we systematically investigated the effects of nanozyme content and laser power density on the photothermal properties of HMAux samples. As shown in Fig. 4C, the temperature of $HMAu_0$ increases from 18.3 °C to 18.5 °C, and the temperature of $HMAu_1$, $HMAu_{1.5}$, and $HMAu_2$ increases from 18.1 °C, 18.4 °C, and 18.6 °C–27.4 °C, 36.4 °C, and 38.4 °C, respectively, after continuous irradiation of the 808 nm laser (1 W/cm^2) for 10 min. The absolute values of the temperature increase are ordered as $HMAu_2 > HMAu_{1.5} > HMAu_1 > HMAu_0$, which indicates that Fe-MIL-$88NH_2$-Au nanozyme has good photothermal properties, and the introduction of Fe-MIL-$88NH_2$-Au nanozyme can impart hydrogel samples good photothermal properties. Similarly, the effect of Fe-MIL-$88NH_2$-Au nanozyme content on the photothermal performance of HMAux was investigated at laser power densities of 1.5 W/cm^2 and 2 W/cm^2, and the results are shown in Fig. 4D and E. It is found that the temperatures are 39.3 °C, 49.3 °C, and 56.3 °C at 1.5 W/cm^2 and 40.1 °C, 53.0 °C, and 69.4 °C at 2

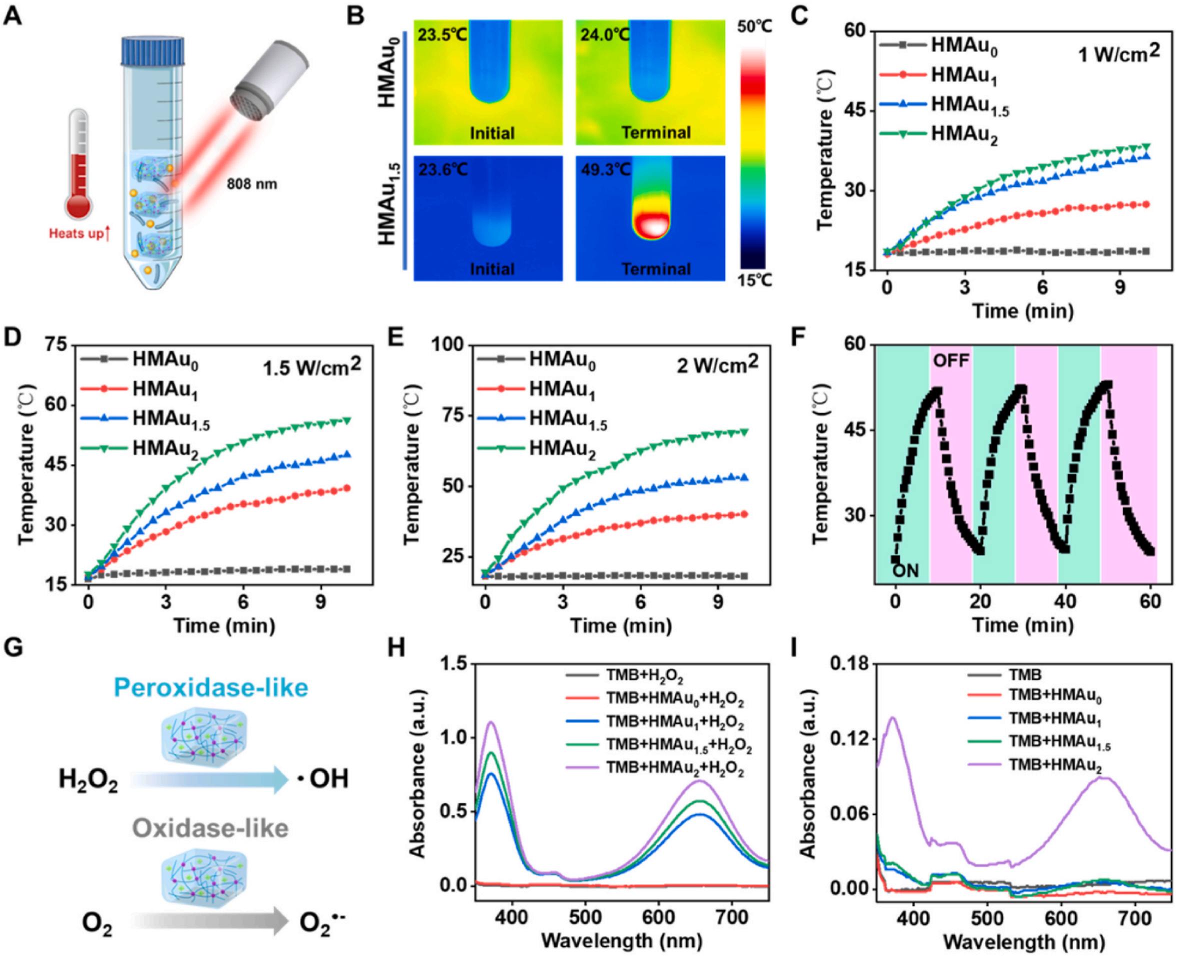

Fig. 4. (A) Schematic diagram of photothermal performance tests of HMAux. (B) Thermal images of $HMAu_0$ and $HMAu_{1.5}$ before and after 10 min with 808 nm laser irradiation. Temperature variation curves of $HMAu_x$ under NIR at (C) 1 W/cm^2, (D) 1.5 W/cm^2, and (E) 2 W/cm^2. (F) On-off temperature change curves for $HMAu_{1.5}$ under NIR irradiation (1.5 W/cm^2). (G) Schematic diagram of •OH and $O_2^{\bullet -}$ generation catalyzed by $HMAu_{1.5}$. UV–vis spectra of different sample systems (H) with and (I) without H_2O_2.

W/cm^2, respectively, when Fe-MIL-88NH$_2$-Au nanozyme content increases from 1 mg/mL to 1.5 mg/mL and then to 2 mg/mL. We have calculated the photothermal conversion efficiency (η) of HMAux [51]. The results are shown in Figures S14. According to the experimental and calculative results, the photothermal conversion efficiency (η) of HMAux is about 55.66 %. After that, we studied the cycling stability of the photothermal properties of HMAux sample. Taking HMAu$_{1.5}$ as an example, we conducted three consecutive laser on-off processes, and the results are shown in Fig. 4F, exhibiting its good photothermal cycling stability.

ROS such as •OH and $O_2^{\bullet -}$ cause irreversible damage to bacteria, leading to bacterial death [52]. The peroxidase and oxidase activities of HMAux determine their abilities to generate free radicals, which directly determines their bactericidal ability. Therefore, the peroxidase-like and oxidase-like activities of HMAux were investigated. As shown in Fig. 4H, HMAu$_0$ cannot oxidize TMB to ox-TMB in the presence of 100 μM H_2O_2, whereas other hydrogel samples containing nanozyme show an enhanced peak signal at 652 nm with the increase of Fe-MIL-88NH$_2$-Au nanozyme, demonstrating the peroxidase-like activity of HMAu$_1$, HMAu$_{1.5}$, and HMAu$_2$. As shown in Fig. 4I, HMAu$_1$, HMAu$_{1.5}$, and HMAu$_2$ can also oxidize TMB to ox-TMB in the absence of H_2O_2, and an enhanced peak signal at 652 nm appears with the increase of Fe-MIL-88NH$_2$-Au nanozyme, effectively demonstrating the oxidase-like activity of HMAu$_1$, HMAu$_{1.5}$, and HMAu$_2$ [37]. We have performed the electron spin resonance tests to confirm the presence of •OH and $O_2^{\bullet -}$ in the systems. As shown in Figure S15, a typical •OH signal peak appeared in the ESR spectrum in HMAu$_{1.5}$/DMPO system when 100 μM H_2O_2 was presented, demonstrating the generation of •OH. And the HMAu$_{1.5}$/DMPO system showed an $O_2^{\bullet -}$ signal peak when H_2O_2 was absented, demonstrating the generation of $O_2^{\bullet -}$ [52,53].

3.4. Dual-mode antibacterial performance of HMAux

To investigate the antibacterial properties of HMAux, the killing effects against *S. aureus* and *E. coli* under different conditions were evaluated by plate coating experiments. Fig. 5A shows the pictures of the bacterial colonies formed by *S. aureus* or *E. coli* treated with 12 different groups, each showing significant differences in antibacterial activity. The specific survival rates of *S. aureus* or *E. coli* are shown in Fig. 5B and C, respectively. In the absence of both NIR laser irradiation and H_2O_2, the mortality rates of *S. aureus* after contact with HMAu$_0$ or HMAu$_{1.5}$ are 11.44 % and 27.36 %, and the mortality rates of *E. coli* are 20.00 % and 51.73 %, respectively. Under the conditions without NIR laser irradiation but with the addition of H_2O_2, the mortality rates of *S. aureus* after contact with HMAu$_0$ or HMAu$_{1.5}$ are 38.64 % and 54.89 %, and the mortality rates of *E. coli* are 40.99 % and 58.89 %, respectively. Under the conditions of NIR laser irradiation but without the addition of H_2O_2, the mortality rates of *S. aureus* after contact with HMAu$_0$ or HMAu$_{1.5}$ are 9.29 % and 56.72 %, and the mortality rates of *E. coli* are 18.27 % and 78.77 %, respectively. Under the condition of both NIR laser irradiation and H_2O_2 addition, the mortality rates of *S. aureus* after contact with HMAu$_0$ or HMAu$_{1.5}$ are 37.56 % and 95.02 %, and the mortality rates of *E. coli* are 39.26 % and 97.28 %, respectively. The results show that HMAu$_{1.5}$ can effectively kill bacteria under NIR laser irradiation and the addition of 100 μM H_2O_2, and has a better killing effect on *E. coli* than *S. aureus*. This is mainly attributed to the differences in cell wall

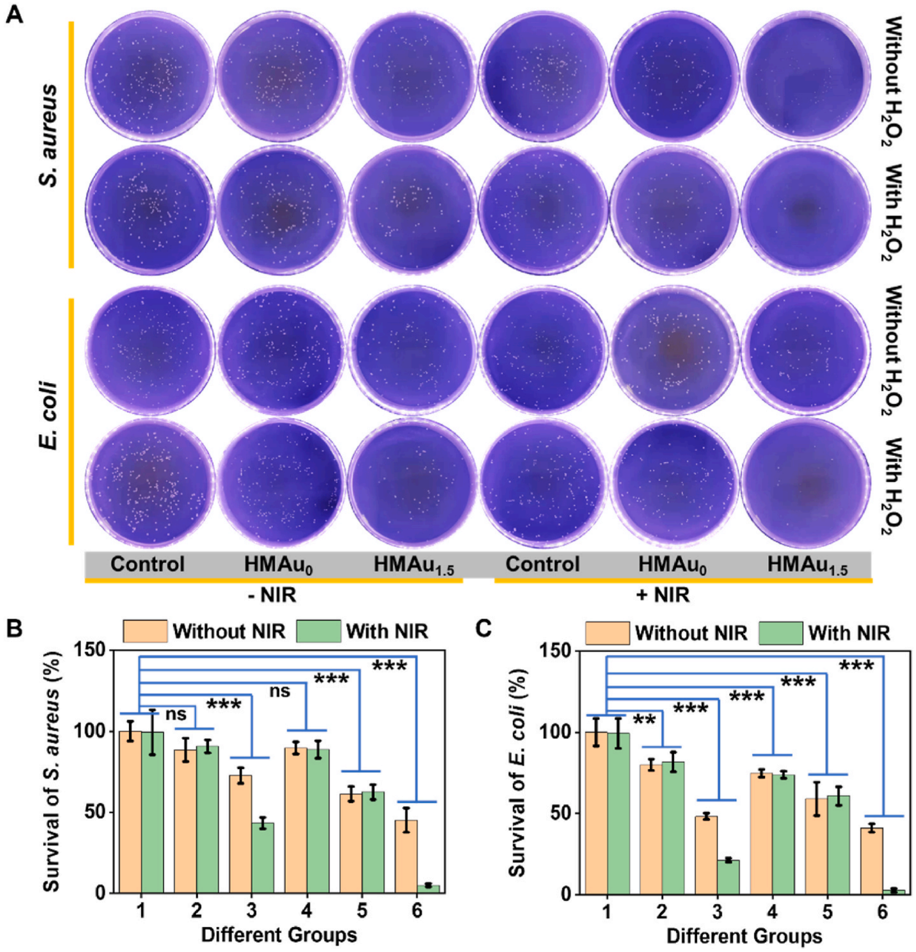

Fig. 5. (A) Photographs of bacterial colonies formed by *S. aureus* or *E. coli* treated with different groups. Survival ratios of (B) *S. aureus* and (C) *E. coli* after being treated by different groups. 1: Control; 2: HMAu$_0$; 3: HMAu$_{1.5}$; 4: Control + H_2O_2; 5: HMAu$_0$+H_2O_2; 6: HMAu$_{1.5}$+H_2O_2.

structure and composition between *S. aureus* and *E. coli*, which leads to differences in tolerance to thermal and oxidative damage as well as acidic conditions. The results of antimicrobial experiments fully demonstrate that $HMAu_{1.5}$ exerts synergistic photothermal and chemodynamic effects, resulting in good antibacterial performance (with killing rates of over 95 % for *S. aureus* and over 97 % for *E. coli*).

3.5. *Application of HMAux in infection wounds*

We attempted to use $HMAu_{1.5}$ as a wound dressing for *in vivo* antibacterial purposes to promote infected wound healing. The pictures of the wound healing process of different treatment groups are shown in Fig. 6A. All groups show various degrees of infection on the second day except for the $HMAux_{1.5}$+H_2O_2 (100 μM) + NIR group, proving that the

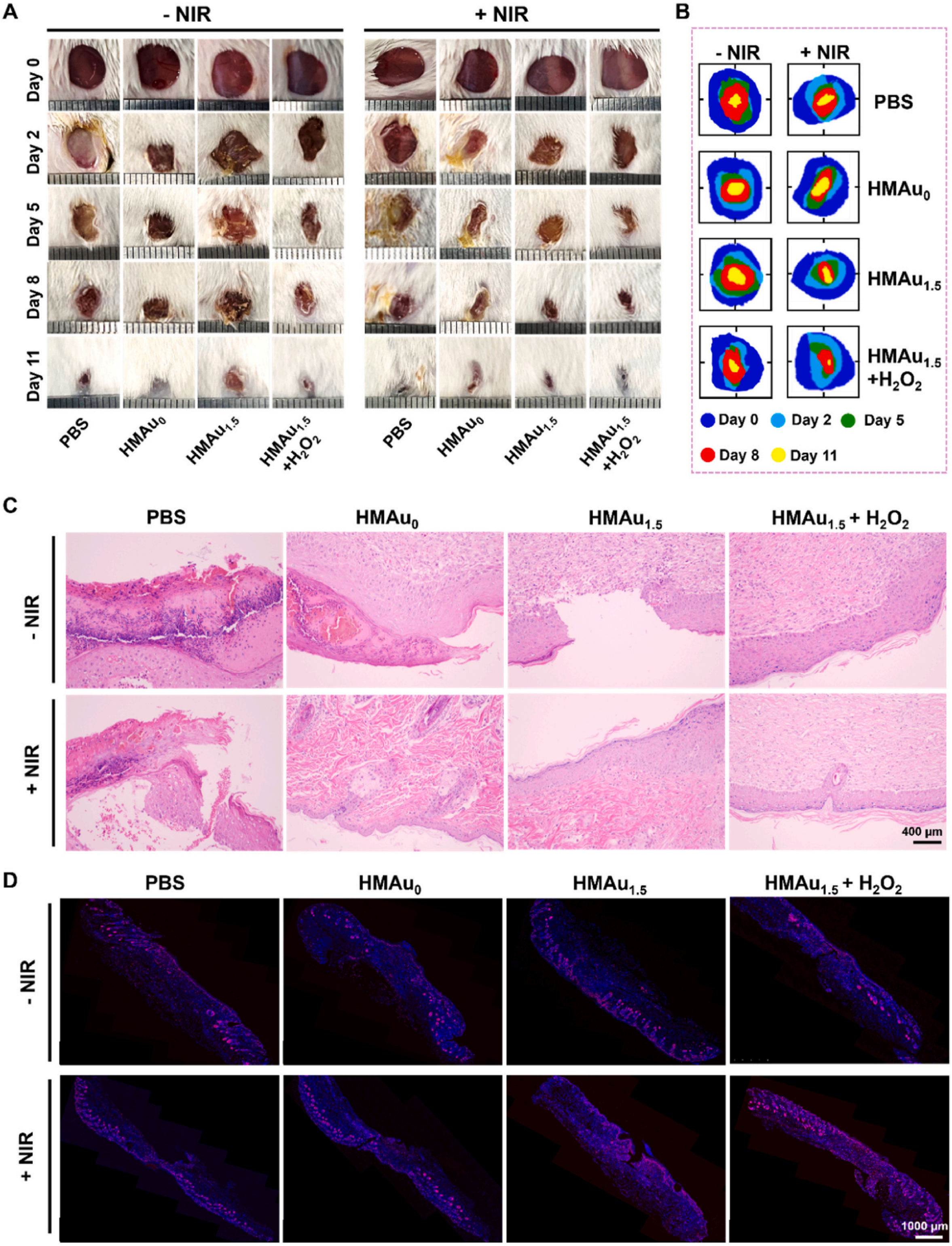

Fig. 6. Efficacy of different sample groups for treating infected wounds. (A) Photographs and (B) traces of wound closure over the 11-day treatment period. (C) Histomorphological assay and (D) immunofluorescence staining of Ki-67 in wounds on day 11 of treatment.

group combining PTT and CDT has the best antibacterial effect. The varying degrees of infection in the other groups gradually subsided on the 5th or even 8th day, which may be related to the gradual recovery of the immune system. We plotted wound healing trajectories within 11 days for different treatment groups to clearly demonstrate the different healing effects, which were shown in Fig. 6B. The results indicate that both HMAu$_{1.5}$+NIR group and HMAu$_{1.5}$+H_2O_2 group can accelerate wound healing, and the combination of HMAu$_{1.5}$ with NIR and H_2O_2 has the best effect on wound healing. It is worth noting that wounds treated with HMAux$_{1.5}$+H_2O_2+NIR can be almost completely covered by newly formed skin on the 11th day.

Furthermore, histological staining was performed to evaluate the effect of different treatment groups on wound healing. After 11 days of treatment, a more complete epithelium and hair follicles were observed in both HMAu$_{1.5}$+NIR group, HMAu$_{1.5}$+H_2O_2 group, and HMAux$_{1.5}$+H_2O_2+NIR group, with the latter group showing the most pronounced healing effect (Fig. 6C). The levels of typical inflammatory factors IL-6 and TNF-α at the wound site were also evaluated (Figures S16 and S17). Compared with the other control groups, the HMAux$_{1.5}$+H_2O_2+NIR group showed a significant decrease in positive staining intensity, indicating a decrease in inflammatory expression. Additionally, Ki-67 is a nuclear protein associated with ribosomal RNA transcription and is used to characterize cell proliferation [54]. Collagen I (COL-I) plays a significant role in the wound healing process [55], mediating several key steps in an integrin signal-dependent manner, such as platelet aggregation, inflammation regulation, angiogenesis, granulation tissue formation, and re-epithelialization. Ki-67 expression was higher in the HMAux$_{1.5}$+H_2O_2+NIR group, indicating greater cell proliferation at the wound site (Fig. 6D). The HMAux$_{1.5}$+H_2O_2+NIR group also showed high levels of COL-I deposition during the healing process, illustrating that it promotes collagen deposition (Figure S18).

3.6. Biocompatibility of HMAux

The *in vitro* biocompatibility of the HMAux samples was preliminarily evaluated through cell experiments. As shown in Fig. 7A, the cell viability of L929 cells after co-culturing with HMAux samples for 24 h is close to 100 %, demonstrating that HMAux samples are virtually non-cytotoxic within 24 h. The same conclusion is reached by live/dead stain tests and morphology assays (Fig. 7B). Cell co-culture assays demonstrate the biosafety of HMAux samples.

In addition, H&E staining was performed on the main organs of mice after different treatments for 11 days to investigate their safety *in vivo*. As shown in Fig. 7C, no significant toxicity is detected in the main organs (heart, liver, spleen, lung, kidney) of any groups, indicating that the material system has good biocompatibility *in vivo*. Therefore, HMAu$_{1.5}$ is expected to have potential value in the treatment and healing of infectious wounds in movable parts.

4. Conclusions

A new class of good stretchability (3244 %–4524 %), toughness (593.8 kJ/m^3 to 421.5 kJ/m^3), and low hysteresis (13.46 %–14.75 %) HMAux was easily prepared by copolymerization of acrylamide and

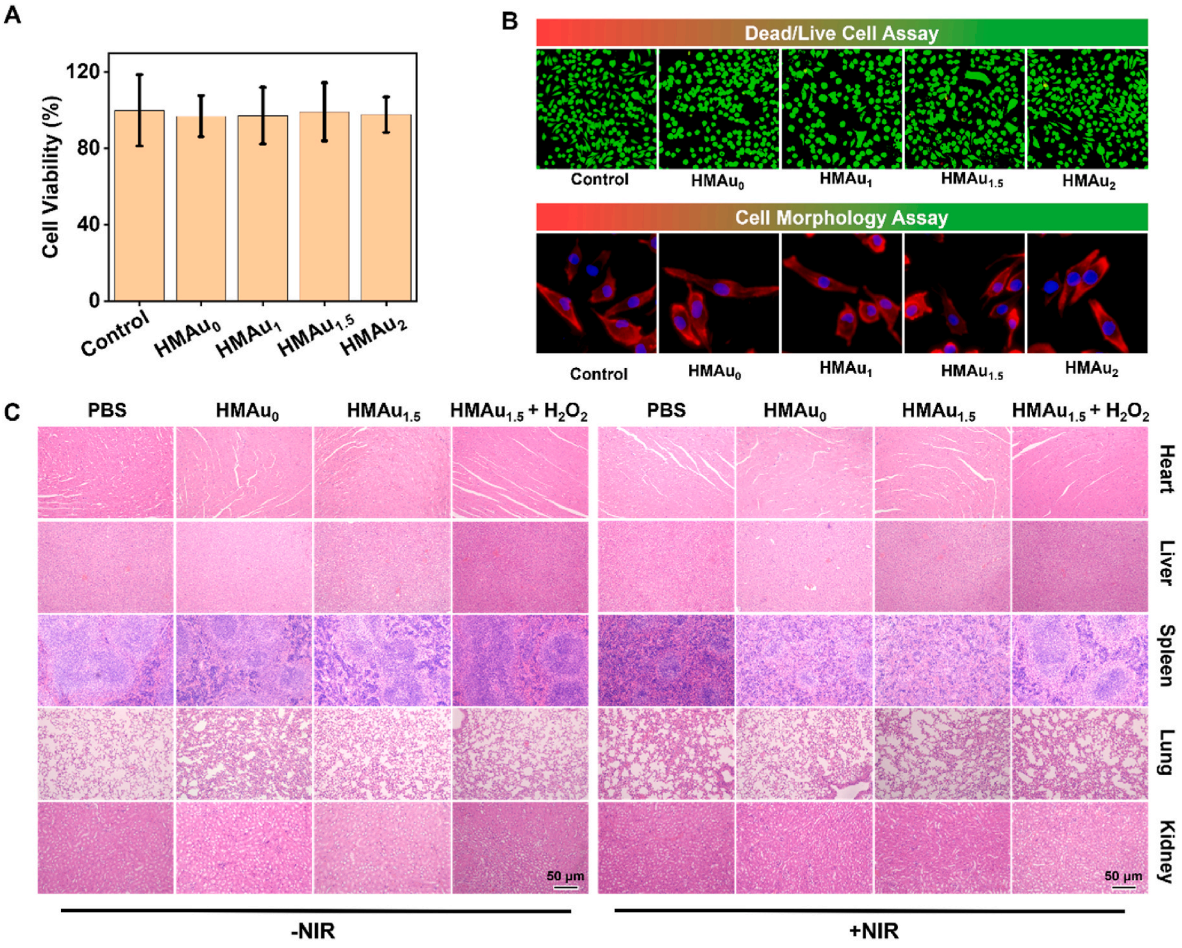

Fig. 7. Biocompatibility assay of HMAux. (A) Cell viability of L929 cells after co-cultured with HMAu$_0$, HMAu$_1$, HMAu$_{1.5}$ and HMAu$_2$ for 24 h. (B) Cell dead/live and morphology assays of L929 cells after co-cultured with HMAu$_0$, HMAu$_1$, HMAu$_{1.5}$ and HMAu$_2$ for 24 h. (C) H&E staining images of the main organs of the mice after 11 days of treatment with different groups.

PF127-DA in aqueous solution containing Fe-MIL-$88NH_2$-Au nanozyme. The design strategy of HMAux employs the PF127-DA dynamic micelle structure to optimize mechanical properties rather than introducing sacrificial bonds, resulting in high toughness and low hysteresis simultaneously. Its excellent mechanical properties can make the material not easy to break and maintain its original shape under the action of external force, effectively blocking external contact with the wound and prevent wound cracking. Besides, the Fe-MIL-$88NH_2$-Au nanozyme as the functional component exhibits photothermal properties and peroxidase-like and oxidase-like activities, endowing HMAux with the abilities of photothermal conversion and ROS production. The synergistic effects of PTT and CDT in HMAux allow them to exhibit good antibacterial performance under mild conditions. We demonstrated that HMAux had a killing rate of approximately 95.02 % against *S. aureus*, and about 97.28 % against *E. coli*. *In vivo* experiments showed that $HMAu_{1.5}$ decreased the expression of inflammatory factors, promoted cell proliferation and collagen deposition, and accelerated wound healing, indicating its potential as a wound dressing for treating wound infections in movable parts.

CRediT authorship contribution statement

Yanyan Li: Writing – original draft, Methodology, Investigation, Funding acquisition, Conceptualization. **Weiqi Kang:** Methodology, Investigation. **Jian Zhang:** Investigation, Funding acquisition. **Ping Shi:** Writing – review & editing, Funding acquisition. **Jianshu Li:** Writing – review & editing, Funding acquisition. **Yongping Lu:** Writing – review & editing, Investigation, Funding acquisition.

Declaration of competing interest

The authors declare that they have no known competing financial interests or personal relationships that could have appeared to influence the work reported in this paper.

Acknowledgments

This work was supported by the Youth Science Foundation of Shanxi Province (202203021222012) and Natural Science Foundation of Shanxi Province (20210302123458). Natural Science Foundation of Sichuan Province (2023NSFSC0329), (2024NSFSC1023). And Health Commission Program of Sichuan Province (24WSXT040), Medical Research Program of Sichuan Province (Q23015).

Appendix A. Supplementary data

Supplementary data to this article can be found online at https://doi.org/10.1016/j.mtbio.2025.101547.

Data availability

Data will be made available on request.

References

[1] S. Cheng, H. Wang, X. Pan, et al., Dendritic hydrogels with robust inherent antibacterial properties for promoting bacteria-infected wound healing, ACS Appl. Mater. Interfaces 14 (9) (2022) 11144–11155.
[2] K. Harding, Chronic wounds: a clinical problem requiring ownership and coordination, Br. J. Dermatol. 187 (2) (2022) 133–134.
[3] X. Qi, X. Ge, X. Chen, et al., An immune regulation hydrogel with controlled hyperthermia-augmented oxygenation and ROS Scavenging for treating diabetic foot ulcers, Adv. Funct. Mater. 34 (2024) 2400489.
[4] X. Qi, E. Cai, Y. Xiang, et al., An immunomodulatory hydrogel by hyperthermia-assisted self-cascade glucose depletion and ROS scavenging for diabetic foot ulcer wound therapeutics, Adv. Mater. 35 (48) (2023) 2306632.
[5] M. Farahani, A. Shafiee, Wound healing: from passive to smart dressings, Adv. Healthcare Mater. 10 (16) (2021) 2100477.
[6] R. Dong, B. Guo, Smart wound dressings for wound healing, Nano Today 41 (2021) 101290.
[7] Y. Lyu, H. Ren, M. Yu, et al., Using oxidized amylose as carrier of linalool for the development of antibacterial wound dressing, Carbohydr. Polym. 174 (2017) 1095–1105.
[8] M. Parani, G. Lokhande, A. Singh, et al., Engineered nanomaterials for infection control and healing acute and chronic wounds, ACS Appl. Mater. Interfaces 8 (16) (2016) 10049–10069.
[9] S. Homaeigohar, A. Boccaccini, Antibacterial biohybrid nanofibers for wound dressings, Acta Biomater. 107 (2020) 25–49.
[10] S. Latiyan, T. Kumar, M. Doble, et al., Perspectives of nanofibrous wound dressings based on glucans and galactans-A review, Int. J. Biol. Macromol. 244 (2023) 125358.
[11] W. Cheng, Y. Zhu, G. Jiang, et al., Sustainable cellulose and its derivatives for promising biomedical applications, Prog. Mater. Sci. 138 (2023) 101152.
[12] X. Qi, Y. Shi, C. Zhang, et al., A hybrid hydrogel with intrinsic immune modulatory functionality for treating multidrug-resistant pseudomonas aeruginosa infected diabetic foot ulcers, ACS Mater. Lett. 6 (2024) 2533–2547.
[13] Y. Liang, J. He, B. Guo, Functional hydrogels as wound dressing to enhance wound healing, ACS Nano 15 (8) (2021) 12687–12722.
[14] Y. Li, J. Wang, Y. Wang, et al., Advanced electrospun hydrogel fibers for wound healing, Compos Part B Eng 223 (2021) 109101.
[15] X. You, X. Wang, H. Zhang, et al., Supertough lignin hydrogels with multienergy dissipative structures and ultrahigh antioxidative activities, ACS Appl. Mater. Interfaces 12 (2020) 39892–39901.
[16] C. Zhang, B. Wu, Y. Zhou, et al., Mussel-inspired hydrogels: from design principles to promising applications, Chem. Soc. Rev. 49 (2020) 3605–3637.
[17] Z. Wang, C. Xiang, X. Yao, et al., Stretchable materials of high toughness and low hysteresis, Proc. Natl. Acad. Sci. U.S.A. 116 (2019) 5967–5972.
[18] J. Gong, Why are double network hydrogels so tough? Soft Matter 6 (2010) 2583–2590.
[19] J. Sun, X. Zhao, W. Illeperuma, et al., Highly stretchable and tough hydrogels, Nature 489 (2012) 133–136.
[20] J. Li, W. Illeperuma, Z. Suo, et al., Hybrid hydrogels with extremely high stiffness and toughness, ACS Macro Lett. 3 (2014) 520–523.
[21] A. Dorost, Y. Safari, M. Akhlaghi, et al., Microbial contamination data of keypad and touch screen of cell phones among hospital and non-hospital staffs-a case study: Iran, Data Brief 20 (2018) 80–84.
[22] X. Qi, Y. Xiang, E. Cai, et al., Inorganic–organic hybrid nanomaterials for photothermal antibacterial therapy, Coord. Chem. Rev. 496 (2023) 215426.
[23] Y. Yang, L. Ma, C. Cheng, et al., Nonchemotherapic and robust dual-responsive nanoagents with on-demand bacterial trapping, ablation, and release for efficient wound disinfection, Adv. Funct. Mater. 28 (2018) 1705708.
[24] Y. Huang, J. Ren, X. Qu, Nanozymes: classification, catalytic mechanisms, activity regulation, and applications, Chem. Rev. 119 (2019) 4357–4412.
[25] J. Sun, L. Song, Y. Fan, et al., Synergistic photodynamic and photothermal antibacterial nanocomposite membrane triggered by single NIR light source, ACS Appl. Mater. Interfaces 11 (2019) 26581–26589.
[26] X. Qi, Y. Huang, S. You, et al., Engineering robust Ag-decorated polydopamine nano-photothermal platforms to combat bacterial infection and prompt wound healing, Adv. Sci. 9 (11) (2022) 2106015.
[27] H. Sun, N. Gao, K. Dong, et al., Graphene quantum dots-band-aids used for wound 62 disinfection, ACS Nano 8 (2014) 6202–6210.
[28] Z. Yuan, C. Lin, Y. He, et al., Near-infrared light-triggered nitric-oxide enhanced photodynamic therapy and low temperature photothermal therapy for biofilm elimination, ACS Nano 14 (2020) 3546–3562.
[29] Z. Chen, Z. Wang, J. Ren, et al., Enzyme mimicry for combating bacteria and biofilms, Acc. Chem. Res. 51 (2018) 789–799.
[30] J. Xu, K. Yao, Z. Xu, Nanomaterials with a photothermal effect for antibacterial activities: an overview, Nanoscale 11 (18) (2019) 8680–8691.
[31] C. Wang, Y. Liang, Y. Huang, et al., Porous photothermal antibacterial antioxidant dual-crosslinked cryogel based on hyaluronic acid/polydopamine for non-compressible hemostasis and infectious wound repair, J. Mater. Sci. Technol. 121 (2022) 207–219.
[32] J. Wu, Y. Wei, J. Lan, et al., Screening of protein-based ultrasmall nanozymes for building cell-mimicking catalytic vesicles, Small 18 (39) (2022) 2202145.
[33] B. Mohanty, S. Kumari, P. Yadav, et al., Metal-organic frameworks (MOFs) and MOF composites based biosensors, Coord. Chem. Rev. 519 (2024) 216102.
[34] Y. Li, P. Yu, J. Wen, et al., Nanozyme-based stretchable hydrogel of low hysteresis with antibacterial and antioxidant dual functions for closely fitting and wound healing in movable parts, Adv. Funct. Mater. 32 (13) (2022) 2110720.
[35] D. Xie, Y. Ma, Y. Gu, et al., Bifunctional NH_2 MIL-88(Fe) metal-organic framework nanooctahedra for highly sensitive detection and efficient removal of arsenate in aqueous media, J. Mater. Chem. A. 5 (2017) 23794–23804.
[36] X. Zhao, B. Guo, H. Wu, et al., Injectable antibacterial conductive nanocomposite cryogels with rapid shape recovery for noncompressible hemorrhage and wound healing, Nat. Commun. 9 (2018) 2784.
[37] Y. Tao, E. Ju, J. Ren, et al., Bifunctionalized mesoporous silica-supported gold nanoparticles: intrinsic oxidase and peroxidase catalytic activities for antibacterial applications, Adv. Mater. 27 (2014) 1097–1105.
[38] S. Wang, H. Zheng, L. Zhou, et al., Nanoenzyme-reinforced injectable hydrogel for healing diabetic wounds infected with multidrug resistant bacteria, Nano Lett. 20 (2020) 5149–5158.
[39] J. Feng, J. Chen, K. Guo, et al., Leeches-inspired hydrogel-elastomer integration materials, ACS Appl. Mater. Interfaces 10 (2018) 40238–40245.

[40] D. Gao, Z. Liu, Z. Cheng, 2D Ni-Fe MOF nanosheets reinforced poly (vinyl alcohol) hydrogels with enhanced mechanical and tribological performance, Colloids Surf., A. 610 (2021) 125934.

[41] X. Fang, Y. Li, X. Li, et al., Dynamic hydrophobic domains enable the fabrication of mechanically robust and highly elastic poly (vinyl alcohol)-based hydrogels with excellent self-healing ability, ACS Mater. Lett. 2 (2020) 764–770.

[42] Y. Cheng, H. Zhu, S. Li, et al., Stretchable, low-hysteresis, and recyclable ionogel by ionic liquid catalyst and mixed ionic liquid-induced phase separation, ACS Sustainable Chem. Eng. 11 (41) (2023) 15031–15042.

[43] R. Du, T. Bao, T. Zhu, et al., A low-hysteresis and highly stretchable ionogel enabled by well dispersed slidable cross-linker for rapid human-machine interaction, Adv. Funct. Mater. 33 (30) (2023) 2212888.

[44] S. Li, Z. Xiao, H. Yang, et al., A skin-inspired anisotropic multidimensional sensor based on low hysteresis organohydrogel with linear sensitivity and excellent robustness for directional perception, Chem. Eng. J. 499 (2024) 156581.

[45] Y. Ye, Y. Zhang, Y. Chen, et al., Cellulose nanofibrils enhanced, strong, stretchable, freezing-tolerant ionic conductive organohydrogel for multi-functional sensors, Adv. Funct. Mater. 30 (35) (2020) 2003430.

[46] Y. Yang, X. Wang, F. Yang, et al., Highly elastic and ultratough hybrid ionic–covalent hydrogels with tunable structures and mechanics, Adv. Mater. 30 (18) (2018) 1707071.

[47] X. Fang, Y. Li, X. Li, et al., Dynamic hydrophobic domains enable the fabrication of mechanically robust and highly elastic poly (vinyl alcohol)-based hydrogels with excellent self-healing ability, ACS Mater. Lett. 2 (7) (2020) 764–770.

[48] S. Shin, Y. Eom, E. Lee, et al., Malleable hydrogel embedded with micellar cargo-expellers as a prompt transdermal patch, Adv. Healthcare Mater. 9 (2020) 2000876.

[49] I. Jeon, J. Cui, W. Illeperuma, et al., Extremely stretchable and fast self-healing hydrogels, Adv. Mater. 28 (2016) 4678–4683.

[50] P. Wang, G. Deng, L. Zhou, et al., Ultrastretchable, self-healable hydrogels based on dynamic covalent bonding and triblock copolymer micellization, ACS Macro Lett. 6 (2017) 881–886.

[51] J. Mei, D. Xu, L. Wang, et al., Biofilm microenvironment-responsive self-assembly nanoreactors for all-stage biofilm associated infection through bacterial cuproptosis-like death and macrophage re-rousing, Adv. Mater. 35 (36) (2023) 2303432.

[52] B. Xu, H. Wang, W. Wang, et al., A single-atom nanozyme for wound disinfection applications, Angew. Chem. 131 (15) (2019) 4965–4970.

[53] M. Cheng, W. Ma, J. Li, et al., Visible-light-assisted degradation of dye pollutants over Fe (III)-loaded resin in the presence of H_2O_2 at neutral pH values, Environ. Sci. Technol. 38 (5) (2004) 1569–1575.

[54] J. Bullwinkel, B. Baron-Lühr, A. Lüdemann, et al., Ki-67 protein is associated with ribosomal RNA transcription in quiescent and proliferating cells, J. Cell. Physiol. 206 (3) (2006) 624–635.

[55] Y. Wang, Y. Zhang, T. Li, et al., Adipose mesenchymal stem cell derived exosomes promote keratinocytes and fibroblasts embedded in collagen/platelet-rich plasma scaffold and accelerate wound healing, Adv. Mater. 35 (40) (2023) 2303642.